Plasmon excitations in graphitic carbon spheres

Thomas Stöckli,* Jean-Marc Bonard, and André Châtelain
*Institut de Physique Expérimentale, Département de Physique, Ecole Polytechnique Fédérale de Lausanne,
CH-1015 Lausanne, Switzerland*

Zhong Lin Wang
School of Materials Science and Engineering, Georgia Institute of Technology, Atlanta, Georgia 30332-0245

Pierre Stadelmann
*Centre Interdépartemental de Microscopie Electronique, Ecole Polytechnique Fédérale de Lausanne,
CH-1015 Lausanne, Switzerland*
(Received 30 January 1998)

Electron energy loss spectroscopy in a high-resolution transmission electron microscope has recently been used with success to characterize the electronic properties of closed cage nanometer-size graphitic particles. In the plasmon region, the experimental data reveal interesting size-dependent variations, which are not yet fully understood. The difficulties encountered in the interpretation of the spectra are principally due to the lack of a complete theoretical treatment of the anisotropic dielectric response in nanometer-size particles. In order to obtain a better understanding of the experimental data we propose a model based on nonrelativistic local dielectric response theory for electrons penetrating through a nested concentric-shell fullerene or the so-called ''carbon onion.'' The anisotropy of the electronic properties of the sphere is taken into account via the frequency-dependent dielectric tensor of graphite. The model can be applied to simulate electron energy loss spectra as well as line scans through energy filtered images and allows thus a direct comparison to experimental data. [S0163-1829(98)04724-9]

I. INTRODUCTION

Since the discovery of the fullerenes by Kroto *et al.*[1] a great variety of molecular carbon structures such as multishell carbon nanotubes,[2,3] multishell fullerenes (also called nested concentric-shelled fullerens or ''carbon onions''),[4] and single shell carbon nanotubes[5,6] have been synthesized. The study of the physical properties of the fullerenes has rapidly developed into an important field of research, mainly because it is possible to produce macroscopic quantities of pure samples.[7] The investigation of the properties of carbon nanotubes and multishell fullerenes has in contrast proven more difficult. Even though important progress has been made recently,[8–10] samples always contain small amounts of impurities, which hamper the characterization of the pure material by methods using macroscopic amounts of samples. In spite of this problem, a lot of effort has been put into the determination of the physical properties of carbon nanotubes and multishell fullerenes, stimulated by theoretical calculations which predict interesting geometry-dependent magnetic[11,12] or electronic properties.[13–23]

For samples containing impurities, experimental methods allowing the investigation of the physical properties on a nanometer-scale are of interest. With methods such as field emission,[24] atomic force,[25] or scanning tunnelling microscopy,[26] some insight into the band structure of carbon nanostructures has recently been achieved. Another powerful method allowing the investigation of the electronic properties of very small amounts of unpurified samples is electron energy loss spectroscopy (EELS) in a high-resolution transmission electron microscope (HRTEM). The high spatial resolution of the HRTEM allows one to select one particle of interest and to determine its shape and dimension. Furthermore, since the electron probe can be focused to a very small diameter, the electronic properties of one single particle can be measured, even as a function of the impact parameter. The technique gives complementary information on those that can be obtained by local probe microscopy. Low loss spectra (losses between 5 and 40 eV) contain information on the collective excitation of the valence electrons (plasmons) and core loss spectra (losses between 40 eV and several keV) contain information on the excitation of the core electrons.

Several experimental studies[27–32] on carbon nanostructures by means of EELS have been reported so far and size-dependent variations of the electronic properties have been observed. By comparison with band structure calculations it was possible to relate the variations in the K-edge spectra of nanotubes of different size to the curvature of the graphitic layers.[32] In the plasmon loss region, however, size-induced variations are still not well understood. Even though several models have been proposed, the comparison of the experimental data with simulations remains difficult. Simulations based upon a hydrodynamic model for tubes and multishell fullerenes[17,18,33] give information about the plasmon dispersion relation, which cannot be measured with EELS in a conventional HRTEM. Density functional theory calculations have been carried out for spherical particles[22] as well as for tubes,[13–16,23] but simulations for more than two concentric layers have not been reported yet, and furthermore the excitation of the plasmon modes by electrons has not been treated. Finally, classical dielectric response theory[19–21] has been used to calculate the excitation probability of plasmons

excited by electrons, however, only for a special case; namely, for nonpenetrating electrons.

We present here a complete treatment of the excitation of plasmons by high-energy electrons in multishell fullerenes based on classical dielectric response theory. The model takes into account the local anisotropy of the dielectric properties of such particles and will allow a detailed comparison with experimental data. Models developed within the frame of classical dielectric response theory[34] have been used with success to interpret plasmon losses in electron energy loss spectroscopy. Such models predict correctly the resonance energies and the intensities of the surface and volume plasmon excitations for different geometries such as thin slabs,[35] spheres,[36–39] layered spheres,[38,40,41] spheres halfway embedded in a supporting medium,[42,43] and cylindrical channels[44–47] and explain size-dependent variations of the peak position. The electronic properties of the material composing the nanoparticle are taken into account via its frequency-dependent dielectric function. For the case of nested concentric-shelled fullerens, the existing calculations for penetrating electrons[39] cannot be used directly since the dielectric function was taken to be isotropic. Multishell fullerenes, however, are composed of concentric spherically curved graphene sheets and it must be assumed that the electronic properties in the directions parallel or perpendicular to the sheets are different, as in the case of planar graphite. In the following sections, the basic ideas of the classical dielectric response theory taking into account this anisotropy are presented (Sec. II) and the expression of the plasmon excitation probability is derived (Sec. III). In Sec. IV simulations of different experiments that can be carried out in a transmission electron microscope equipped with an energy filter are presented and discussed.

II. CLASSICAL ELECTRON ENERGY LOSS THEORY

A. General considerations

Due to the Coulomb interaction, the electrons of a TEM probe are subject to both elastic and inelastic scattering as they pass through the sample. EELS consists in measuring and analyzing the energy loss of the inelastically scattered electrons. In this paper, we focus on the analysis of low loss EEL spectra (up to 40 eV), in which the energy loss can be attributed to the excitation of plasmons, either in the bulk or at the surface of the particle.

An incident electron is treated as a classical particle. In a typical EELS configuration, an electron flux of about 10^{12} electrons per second passes through the sample. Given the high speed of the electrons, the distance between successive electrons is large enough that the interaction between successive scattering events can be neglected.[48] Plasmon losses can therefore be treated as a single electron scattering process. As the electron moves along its trajectory, it loses parts of its kinetic energy since the potential distribution $V(\mathbf{r},t)$ in the system probe-electron particle generates an electric field $\mathbf{E}(\mathbf{r},t)$ which tends to slow down the electron. The potential can be determined from the Maxwell equations so that the work done by the force $\mathbf{F}(\mathbf{r},t)$ acting on the electron, and thus the energy loss can be evaluated:

$$\Delta E = \int_{\text{trajectory}} \mathbf{F}(\mathbf{x},t)\ \mathbf{dx} = \int_{\text{trajectory}} (-e)\mathbf{E}(\mathbf{x},t)\ \mathbf{dx}. \quad (1)$$

For the solution of the Maxwell equations the phenomenological relation between the electric field $\mathbf{E}(\mathbf{r},t)$ and the displacement field $\mathbf{D}(\mathbf{r},t)$ must be written. Within this macroscopic formalism, the electronic properties of the different media of the system are taken into account via their complex dielectric tensor. The dielectric tensor is known as a function of frequency and wave vector so that it is necessary to solve the Maxwell equations in frequency space. For this reason the Fourier transform of the electric field is introduced in Eq. (1).

$$\Delta E = -\frac{e}{2\pi} \int_{\text{trajectory}} \left(\int_{-\infty}^{\infty} e^{-i\omega t} \mathbf{E}(\mathbf{x},\omega)\ d\omega \right) \mathbf{dx} \quad (2)$$

Note that we adopt the following convention for the Fourier transform from frequency into time space and from time into frequency space:

$$A(\mathbf{r},t) = \frac{1}{2\pi} \int_{-\infty}^{\infty} e^{-i\omega t} A(\mathbf{r},\omega)\ d\omega, \quad (3a)$$

$$A(\mathbf{r},\omega) = \int_{-\infty}^{\infty} e^{i\omega t} A(\mathbf{r},t)\ dt. \quad (3b)$$

Since the relative change in energy and momentum following the interaction with the sample is very small, the electron with a kinetic energy typically higher than 100 keV can be assumed to move at constant velocity on a straight line, so that the path integral in Eq. (2) can be evaluated. The work done by the electric field is equivalent to the energy loss of the electron and can be related to the excitation probability via the relation

$$\Delta E = \int_0^{\infty} \hbar\omega \frac{dP(\omega)}{d\omega} d\omega. \quad (4)$$

B. Determination of the potential $V(\mathbf{r},\omega)$

In classical dielectric theory, the response of a nonisotropic medium to an external electric field is described via the dielectric tensor $\widetilde{\epsilon}(\mathbf{r},\omega)$:

$$\mathbf{D}(\mathbf{r},t) = \epsilon_0 \int_{-\infty}^{\infty} dt' \int_{-\infty}^{\infty} d^3r'\ \widetilde{\epsilon}(\mathbf{r}-\mathbf{r}',t-t')\mathbf{E}(\mathbf{r}',t'). \quad (5)$$

This homogeneous description of the medium is valid if the wave length of the excitation generated by the probe electrons is greater than the interatomic distance. This condition is generally satisfied for plasmons, since their resonance energies are located at energies below 40 eV.

For mathematical convenience, most of the analysis of low loss EEL spectra in terms of classical dielectric theory is done assuming local response of the dielectric medium. In spite of this simplification the model has had considerable success in explaining energy loss spectra of small particles of

different geometries. For this reason, we assume local response in the following calculations. The dielectric tensor in this case takes the form

$$\widetilde{\epsilon}(\mathbf{r}-\mathbf{r}',\omega)=\delta(\mathbf{r}-\mathbf{r}')\widetilde{\epsilon}(\omega) \qquad (6)$$

and Eq. (5) written in frequency space becomes

$$\mathbf{D}(\mathbf{r},\omega)=\epsilon_0\int_{-\infty}^{\infty}d^3r'\ \widetilde{\epsilon}(\mathbf{r}-\mathbf{r}',\omega)\mathbf{E}(\mathbf{r}',\omega)=\epsilon_0\widetilde{\epsilon}(\omega)\mathbf{E}(\mathbf{r},\omega).$$
$$(7)$$

In the simpler isotropic case, the Maxwell equations together with the phenomenological relation between the electric and the displacement field [Eq. (7)] and with the definition of the electric potential $\mathbf{E}(\mathbf{r},\omega)=-\nabla V(\mathbf{r},\omega)$ lead to the following expression for the potential distribution[34,35] which is needed to calculate the electron energy loss probability [Eq. (2)]:

$$\nabla^2 V(\mathbf{r},\omega)=-\frac{1}{\epsilon_0\epsilon(\omega)}\rho(\mathbf{r},\omega). \qquad (8)$$

If the medium is anisotropic, Maxwell equations lead to the following expression determining the electric potential:

$$\nabla\cdot[\epsilon_0\widetilde{\epsilon}(\omega)\nabla V(\mathbf{r},\omega)]=-\rho(\mathbf{r},\omega). \qquad (9)$$

In Eqs. (8) and (9), $\epsilon(\omega)$ and $\widetilde{\epsilon}(\omega)$ are the dielectric function and the dielectric tensor, respectively. $\rho(\mathbf{r},\omega)$ is the charge density due to the probe electron written in frequency space. If the electron is moving at constant velocity v at a given impact parameter x_0 along the z axis, $\rho(\mathbf{r},\omega)$ is given by

$$\rho(\mathbf{r},\omega)=-\frac{e}{v}\delta(x-x_0)\delta(y)e^{i\omega z/v}. \qquad (10)$$

The general solution of Eqs. (8) or (9) is a linear combination of the homogeneous and of the particular solution of the equation. In EELS problems, the particular solution represents the direct potential and is therefore responsible for the volume plasmon, whereas the homogeneous term represents the induced potential and is responsible for the surface loss. In our approach, the two contributions to the energy loss probability are treated separately. First, we calculate the induced potential and the surface excitation probability (Sec. III B). In this case, Eqs. (2) and (4) can be combined to yield the following expression for the surface plasmon excitation probability:[34]

$$\frac{dP^{\mathrm{surf}}(\omega)}{d\omega}=\frac{e}{\pi\hbar v^2}\int_{-\infty}^{\infty}dz'\int_{-\infty}^{\infty}dz$$
$$\times\mathrm{Im}\{e^{i\omega(z'-z)/v}V^{\mathrm{ind}}(\mathbf{r},\mathbf{r}_0)|_{\mathbf{r}=(x_0,0,z')}\}.$$
$$(11)$$

$V^{\mathrm{ind}}(\mathbf{r},\mathbf{r}_0)$ is the induced electric potential at position $\mathbf{r}$ caused by a stationary electron located at position $\mathbf{r}_0=(x_0,0,z)$. In other terms, $V^{\mathrm{ind}}(\mathbf{r},\mathbf{r}_0)$ is the homogeneous part of the solution of

$$\nabla^2 V(\mathbf{r},\mathbf{r}_0)=\frac{e}{\epsilon_0\epsilon(\omega)}\delta(\mathbf{r}-\mathbf{r}_0) \qquad (12)$$

if the electron is traveling in a isotropic medium and of

$$\nabla\cdot[\widetilde{\epsilon}(\omega)\nabla V(r,\mathbf{r}_0)]=\frac{e}{\epsilon_0}\delta(\mathbf{r}-\mathbf{r}_0) \qquad (13)$$

if it is in an anisotropic medium. It is important to note that $V^{\mathrm{ind}}(\mathbf{r},\mathbf{r}_0)$ depends on ω. The potential distribution in space is a quasielectrostatic potential for each point along the trajectory of the incident electron and the integral over z is a sum over the contributions of all the points along the trajectory of the incident electron.

In the second step, we calculate the volume excitation probability (Sec. III C). It would be possible to derive it from the inhomogeneous part of the solutions of Eqs. (8) and (9) eliminating ΔE in Eqs. (2) and (4) and using the fact that $\mathbf{E}(\mathbf{r},t)=-\nabla V(\mathbf{r},t)$. It has, however, turned out to be easier to adapt the results of Wessjohann,[49] who calculated the energy loss probability for uniaxial crystals, to our geometry.

III. DETERMINATION OF THE SURFACE AND VOLUME PLASMON EXCITATION PROBABILITY

A. Modeling the dielectric properties of multishell fullerenes

The multishell fullerenes that we want to model consist of concentric spherical graphene shells with a central cavity.[4] For mathematical convenience we make abstraction of the inner hollow and assume that the shells continue to the center of the sphere. Surface excitations on the inner surface and coupling modes between the inner and the outer surface are therefore ignored. This is an approximation which is reasonable at least for large multishell fullerenes with a small inner cavity, since due to screening, the effects of the inner surface can be expected to be small. A second consequence of this simplification is that the volume contribution to the plasmon excitation probability is overestimated for electrons passing through the center of the sphere. This overestimation could, however, easily be corrected by adapting the integration over the electron trajectory (see Sec. III C).

The model of the dielectric response of a multishell fullerene is based on the dielectric tensor of planar graphite. This tensor takes the form of a diagonal matrix with two different components along the natural cristallographic directions as shown in Fig. 1(a):

$$\widetilde{\epsilon}(\omega)=\epsilon_{\perp}(\omega)\mathbf{e}_{xx}+\epsilon_{\perp}(\omega)\mathbf{e}_{yy}+\epsilon_{\parallel}(\omega)\mathbf{e}_{zz}. \qquad (14)$$

$\epsilon_{\perp}(\omega)$ and $\epsilon_{\parallel}(\omega)$ describe the dielectric response of graphite for an electric field perpendicular and parallel to the c axis, respectively. Several possible ways of describing the dielectric properties of nested concentric-shelled fullerenes based on the dielectric tensor of planar graphite have been proposed and discussed by Lucas.[20,21] From purely geometric considerations, the projection of the dielectric tensor of planar graphite into spherical coordinates

$$\widetilde{\epsilon}(\omega)=\epsilon_{\parallel}(\omega)\mathbf{e}_{rr}+\epsilon_{\perp}(\omega)\mathbf{e}_{\theta\theta}+\epsilon_{\perp}(\omega)\mathbf{e}_{\varphi\varphi} \qquad (15)$$

is most convenient for multishell fullerenes [Fig. 1(b)] and is therefore used in the following calculations.
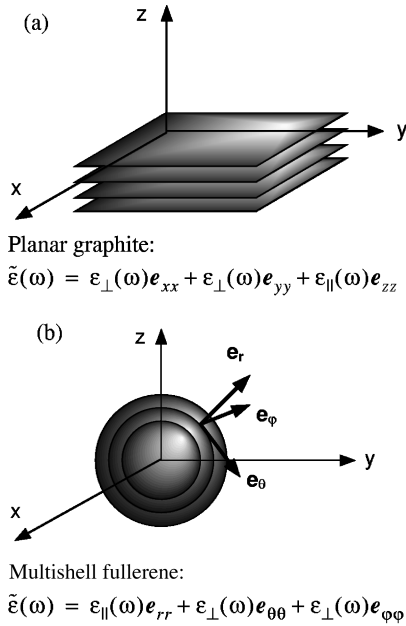
THOMAS STÖCKLI *et al.*

FIG. 1. Dielectric tensor for (a) planar graphite and (b) for the model of a multishell fullerene. For the latter case, the dielectric tensor of graphite is projected into spherical coordinates.

B. Surface plasmon excitation

The problem consists in finding the solution of Eqs. (12) and (13) for the geometry shown in Fig. 2. The sphere of radius a is at the origin of the Cartesian coordinate system xyz. The probe electron, located at position $\mathbf{r}_0$, is parametrized in spherical coordinates r_0, θ_0, and φ_0. Due to symmetry, φ_0 can be chosen to be equal to 0. Since it is assumed that the electron is moving on a straight line at an impact parameter x_0 from the z axis, r_0 and θ_0 can be expressed as a function of the impact parameter and z: $r_0=(z^2+x_0^2)^{1/2}$ and $\cos(\theta_0)=z/r_0$.

For the determination of the potential, the case where the electron is outside the sphere and the case where the electron is inside the sphere need to be treated separately. The potentials for either case are denoted as $V^{\text{in}}(\mathbf{r},\mathbf{r}_0)$ and $V^{\text{out}}(\mathbf{r},\mathbf{r}_0)$, respectively.
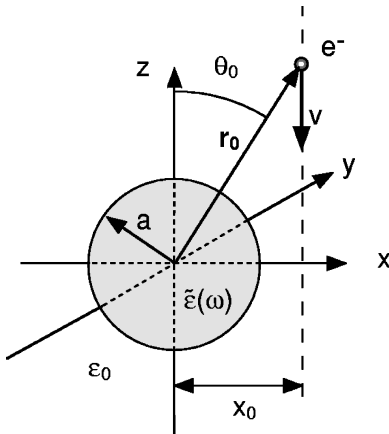

FIG. 2. Geometric definitions for the multishell fullerene geometry. The electron, located at position $\mathbf{r}_0$, is traveling at constant velocity at an impact parameter x_0 from the origin in the negative z direction. In spherical coordinates, its position is given by the parameters r_0, θ_0, and φ_0.

1. Potential distribution for probe electron outside the sphere

The equations that determine the potential distribution for an electron traveling outside the sphere are

$$\nabla^2 V^{\text{out}}_{r>a}(\mathbf{r},\mathbf{r}_0)=\frac{e}{\epsilon_0}\delta(\mathbf{r},\mathbf{r}_0) \qquad (16a)$$

for $r>a$, and

$$\nabla\cdot[\widetilde{\epsilon}(\omega)\nabla V^{\text{out}}_{r<a}(\mathbf{r},\mathbf{r}_0)]=0 \qquad (16b)$$

for $r<a$. The general solution of Eq. (16a) can be written as the sum of homogeneous solution $V^{\text{out,ind}}(\mathbf{r},\mathbf{r}_0)$ (induced potential) and a particular solution of the inhomogeneous equation $V^{\text{out,p}}(\mathbf{r},\mathbf{r}_0)$ (direct potential)

$$V^{\text{out}}_{r>a}(\mathbf{r},\mathbf{r}_0)=V^{\text{out,ind}}_{r>a}(\mathbf{r},\mathbf{r}_0)+V^{\text{out,p}}_{r>a}(\mathbf{r},\mathbf{r}_0). \qquad (17)$$

Equation (16a) with the inhomogeneous term representing a point charge located at $\mathbf{r}_0$ is frequently encountered in classical electrodynamics and its particular solution is

$$V^{\text{out,p}}_{r>a}(\mathbf{r},\mathbf{r}_0)=-\frac{e}{4\pi\epsilon_0|\mathbf{r}-\mathbf{r}_0|}. \qquad (18)$$

For our problem, this solution is rewritten in terms of spherical harmonics.[50,51] For $r<r_0$

$$V^{\text{out,p}}_{r>a}(\mathbf{r},\mathbf{r}_0)=-\frac{e}{4\pi\epsilon_0 r_0}\sum_{l=0}^{\infty}\sum_{m=0}^{l}N_{l,m}(2-\delta_{0,m})\left(\frac{r}{r_0}\right)^l$$
$$\times P_{l,m}[\cos(\theta)]P_{l,m}[\cos(\theta_0)]\cos(m\varphi), \qquad (19)$$

where

$$N_{l,m}=\frac{(l-m)!}{(l+m)!}.$$

If $r>r_0$, r and r_0 are exchanged. $P_{l,m}$ in Eq. (19) denotes the associated Legendre function.

The homogeneous solution of Eq. (16a) is written in the form of an expansion into spherical harmonics with coefficients $A_{l,m}$ that will be determined by the boundary conditions

$$V^{\text{out,ind}}_{r>a}(\mathbf{r},\mathbf{r}_0)=\sum_{l=0}^{\infty}\sum_{m=0}^{l}A_{l,m}(2-\delta_{0,m})$$
$$\times\left(\frac{a}{r}\right)^{l+1}P_{l,m}[\cos(\theta)]\cos(m\varphi). \qquad (20)$$

The solution of the homogeneous equation describing the potential in the anisotropic medium [Eq. (16b)] can also be written in the form of an expansion into spherical harmonics similar to Eq. (20). In fact, in spherical coordinates, the radial equation is found to be

$$r^2\frac{d^2}{dr^2}V(r)+2r\frac{d}{dr}V(r)-\frac{\epsilon_{\perp}(\omega)}{\epsilon_{\parallel}(\omega)}l(l+1)V(r)=0. \qquad (21)$$

If the effective azimuthal quantum number u defined by

$$u(u+1) = \frac{\epsilon_\perp(\omega)}{\epsilon_\parallel(\omega)} l(l+1) \qquad (22)$$

is introduced, Eq. (21) becomes identical to the radial equation in the isotropic case. The solution of the homogeneous equation in the anisotropic case can therefore be obtained from the solution of the isotropic case [Eq. (20)] by replacing the orbital number l in Eq. (20) by $u_l^+(\omega) = 1/2\{-1 + [1 + 4l(l+1)\epsilon_\perp(\omega)/\epsilon_\parallel(\omega)]^{1/2}\}$,[20,21] so that $V^{\text{out, ind}}(\mathbf{r},\mathbf{r}_0)$ becomes

$$V_{r<a}^{\text{out,ind}}(\mathbf{r},\mathbf{r}_0) = \sum_{l=0}^{\infty} \sum_{m=0}^{l} B_{l,m}(2-\delta_{0,m})$$

$$\times \left(\frac{r}{a}\right)^{u_l^+(\omega)} P_{l,m}[\cos(\theta)]\cos(m\varphi). \qquad (23)$$

As in Eq. (20), the coefficients $B_{l,m}$ are unknown and are going to be determined by the boundary conditions.

The homogeneous and particular solutions of Eqs. (16a) and (16b) being known, the general solutions can be written

$$V_{r>a}^{\text{out}}(\mathbf{r},\mathbf{r}_0) = \sum_{l=0}^{\infty} \sum_{m=0}^{l} A_{l,m}(2-\delta_{0,m})$$

$$\times \left(\frac{a}{r}\right)^{l+1} P_{l,m}[\cos(\theta)]\cos(m\varphi)$$

$$-\frac{e}{4\pi\epsilon_0 r_0} \sum_{l=0}^{\infty} \sum_{m=0}^{l} N_{l,m}(2-\delta_{0,m})$$

$$\times \left(\frac{r}{r_0}\right)^{l} P_{l,m}[\cos(\theta)]P_{l,m}[\cos(\theta_0)]\cos(m\varphi),$$

$$(24a)$$

$$V_{r<a}^{\text{out}}(\mathbf{r},\mathbf{r}_0) = \sum_{l=0}^{\infty} \sum_{m=0}^{l} B_{l,m}(2-\delta_{0,m})$$

$$\times \left(\frac{r}{a}\right)^{u_l^+(\omega)} P_{l,m}[\cos(\theta)]\cos(m\varphi). \qquad (24b)$$

The boundary conditions, namely, that the potential and the normal component of the displacement field must be continuous at the sphere surface

$$V_{r>a}^{\text{out}}(\mathbf{r},\mathbf{r}_0)|_{r=a} = V_{r<a}^{\text{out}}(\mathbf{r},\mathbf{r}_0)|_{r=a} \qquad (25a)$$

and

$$\left.\frac{dV_{r>a}^{\text{out}}(\mathbf{r},\mathbf{r}_0)}{dr}\right|_{r=a} = \epsilon_\parallel(\omega)\left.\frac{dV_{r<a}^{\text{out}}(\mathbf{r},\mathbf{r}_0)}{dr}\right|_{r=a} \qquad (25b)$$

lead to the following expression for the coefficients $A_{l,m}$ and $B_{l,m}$:

$$A_{l,m} = f_{l,m}\frac{l-\epsilon_\parallel(\omega)u_l^+(\omega)}{\epsilon_\parallel(\omega)u_l^+(\omega)+(l+1)}, \qquad (26a)$$

$$B_{l,m} = f_{l,m}\frac{2l+1}{\epsilon_\parallel(\omega)u_l^+(\omega)+(l+1)}, \qquad (26b)$$

where

$$f_{l,m} = -\frac{e}{4\pi\epsilon_0 r_0}N_{l,m}P_{l,m}[\cos(\theta_0)]\left(\frac{a}{r_0}\right)^{l}. \qquad (26c)$$

2. Potential distribution for probe electron inside the sphere

The equations that govern the potential distribution when the electron is traveling inside the sphere are

$$\nabla^2 V_{r>a}^{\text{in}}(\mathbf{r},\mathbf{r}_0) = 0 \qquad (27a)$$

for $r>a$ and

$$\nabla\cdot[\widetilde{\epsilon}(\omega)\nabla V_{r<a}^{\text{in}}(\mathbf{r},\mathbf{r}_0)] = -\frac{1}{\epsilon_0}\rho(\mathbf{r},\mathbf{r}_0) \qquad (27b)$$

for $r<a$. The solution of the homogeneous Eq. (27a) can be written in terms of spherical harmonics with coefficients $C_{l,m}$ that are determined by the boundary conditions

$$V_{r>a}^{\text{in}}(\mathbf{r},\mathbf{r}_0) = \sum_{l=0}^{\infty} \sum_{m=0}^{l} C_{l,m}(2-\delta_{0,m})$$

$$\times \left(\frac{a}{r}\right)^{l+1} P_{l,m}[\cos(\theta)]\cos(m\varphi). \qquad (28a)$$

The solution of Eq. (27b) can, as before, be written as the sum of the homogeneous and the inhomogeneous solution:

$$V_{r<a}^{\text{in}}(\mathbf{r},\mathbf{r}_0) = V_{r<a}^{\text{in,p}}(\mathbf{r},\mathbf{r}_0) + V_{r<a}^{\text{in,ind}}(\mathbf{r},\mathbf{r}_0)$$

$$= V_{r<a}^{\text{in,p}}(\mathbf{r},\mathbf{r}_0) + \sum_{l=0}^{\infty} \sum_{m=0}^{l} D_{l,m}(2-\delta_{0,m})$$

$$\times \left(\frac{r}{a}\right)^{u_l^+(\omega)} P_{l,m}[\cos(\theta)]\cos(m\varphi), \qquad (28b)$$

where we have directly introduced the spherical harmonics expansion for the homogeneous term. At this point it has to be noted that it is not necessary to know explicitly the expression of $V^{\text{in,p}}(\mathbf{r},\mathbf{r}_0)$ to determine the surface plasmon excitation probability [Eq. (11)]. In fact, only the induced potential is needed for the evaluation of Eq. (11). The coefficients $C_{l,m}$ and $D_{l,m}$ which determine the induced potential can be calculated most easily via the electric field rather than the potential. In terms of the electric field the solution of Eqs. (27a) and (27b) are

$$\mathbf{E}_{r>a}^{\text{in}}(\mathbf{r},\mathbf{r}_0) = -\nabla V_{r>a}^{\text{in}}(\mathbf{r},\mathbf{r}_0) \qquad (29a)$$

and

$$\mathbf{E}_{r<a}^{\text{in}}(\mathbf{r},\mathbf{r}_0) = -\nabla V_{r<a}^{\text{in}}(\mathbf{r},\mathbf{r}_0)$$

$$= -\nabla V_{r<a}^{\text{in,p}}(\mathbf{r},\mathbf{r}_0) - \nabla V_{r<a}^{\text{in,ind}}(\mathbf{r},\mathbf{r}_0)$$

$$= \mathbf{E}_{r<a}^{\text{in,p}}(\mathbf{r},\mathbf{r}_0) - \nabla V_{r<a}^{\text{in,ind}}(\mathbf{r},\mathbf{r}_0). \qquad (29b)$$

$\mathbf{E}_{r<a}^{\mathrm{in,p}}(\mathbf{r},\mathbf{r}_0)$ is the electric field of a point charge in a infinite anisotropic medium described by the dielectric tensor given in Eq. (15). For $r>r_0$ it can be found to be (see Appendix)

$$\mathbf{E}_{r<a}^{\mathrm{in,p}}(\mathbf{r},\mathbf{r}_0)=\frac{e}{4\pi\epsilon_0}\sum_{l=0}^{\infty}\sum_{m=0}^{l}N_{l,m}(2-\delta_{0,m})P_{l,m}[\cos(\theta_0)]$$

$$\times\left\{-\frac{l+1}{\epsilon_\|(\omega)}\frac{r_0^l}{r^{l+2}}P_{l,m}[\cos(\theta)]\cos(m\varphi)\mathbf{e}_r\right.$$

$$+\frac{1}{\epsilon_\perp(\omega)}\frac{r_0^l}{r^{l+2}}\frac{\partial P_{l,m}[\cos(\theta)]}{\partial\theta}\cos(m\varphi)\mathbf{e}_\theta$$

$$-\frac{1}{\epsilon_\perp(\omega)}\frac{r_0^l}{r^{l+2}}\frac{1}{\sin(\theta)}$$

$$\left.\times P_{l,m}[\cos(\theta)]m\sin(m\varphi)\mathbf{e}_\varphi\right\}. \tag{30}$$

The boundary conditions involving the explicit expression of the potential can now be replaced by the continuity of the tangential component of the electric field and the continuity of the normal component of the displacement vector

$$\mathbf{E}_{r<a}^{\mathrm{in}}(\mathbf{r},\mathbf{r}_0)\cdot\mathbf{e}_\theta|_{r=a}=\mathbf{E}_{r>a}^{\mathrm{in}}(\mathbf{r},\mathbf{r}_0)\cdot\mathbf{e}_\theta|_{r=a}, \tag{31a}$$

$$\mathbf{E}_{r<a}^{\mathrm{in}}(\mathbf{r},\mathbf{r}_0)\cdot\mathbf{e}_\varphi|_{r=a}=\mathbf{E}_{r>a}^{\mathrm{in}}(\mathbf{r},\mathbf{r}_0)\cdot\mathbf{e}_\varphi|_{r=a}, \tag{31b}$$

$$\epsilon_\|(\omega)(\mathbf{E}_{r<a}^{\mathrm{in}}(\mathbf{r},\mathbf{r}_0)\cdot\mathbf{e}_r)|_{r=a}=\mathbf{E}_{r>a}^{\mathrm{in}}(\mathbf{r},\mathbf{r}_0)\cdot\mathbf{e}_r|_{r=a}, \tag{31c}$$

where $\mathbf{E}_{r<a}^{\mathrm{in}}(\mathbf{r},\mathbf{r}_0)\cdot\mathbf{e}_r$, $\mathbf{E}_{r<a}^{\mathrm{in}}(\mathbf{r},\mathbf{r}_0)\cdot\mathbf{e}_\theta$ and $\mathbf{E}_{r<a}^{\mathrm{in}}(\mathbf{r},\mathbf{r}_0)\cdot\mathbf{e}_\varphi$ are the components in spherical coordinates of the electric field inside and outside the particle, respectively. Using these boundary conditions, the coefficients $C_{l,m}$ and $D_{l,m}$ that determine the homogeneous solution of the problem are deduced:

$$C_{l,m}=g_{l,m}\frac{\epsilon_\|(\omega)u_l^+(\omega)+(l+1)\epsilon_\perp(\omega)}{\epsilon_\perp(\omega)[\epsilon_\|(\omega)u_l^+(\omega)+l+1]},$$

$$D_{l,m}=g_{l,m}\frac{(l+1)(\epsilon_\perp(\omega)-1)}{\epsilon_\perp(\omega)[\epsilon_\|(\omega)u_l^+(\omega)+l+1]}, \tag{32a}$$

where

$$g_{l,m}=-\frac{e}{4\pi\epsilon_0 a}N_{l,m}P_{l,m}[\cos(\theta_0)]\left(\frac{r_0}{a}\right)^l. \tag{32b}$$

3. Surface plasmon excitation probability

In the preceding section, the potential was calculated for any possible configuration. Now, the expression for the excitation probability [Eq. (11)] needs to be evaluated. Taking into account the different functions of the potential in the different space regions, the following expression is obtained:

$$\frac{dP^{\mathrm{surf}}(\omega)}{d\omega}=\frac{e}{\pi\hbar v^2}\mathrm{Im}\left[\left\{\int_{-\infty}^{-z_0}dz\,e^{-i\omega z/v}\left(\int_{-\infty}^{-z_0}dz'\,e^{i\omega z'/v}V_{r>a}^{\mathrm{out,ind}}(\mathbf{r},\mathbf{r}_0)+\int_{-z_0}^{z_0}dz'\,e^{i\omega z'/v}V_{r>a}^{\mathrm{in,ind}}(\mathbf{r},\mathbf{r}_0)\right.\right.\right.$$

$$+\int_{z_0}^{\infty}dz'\,e^{i\omega z'/v}V_{r>a}^{\mathrm{out,ind}}(\mathbf{r},\mathbf{r}_0)\Bigg)+\int_{-z_0}^{z_0}dz\,e^{-i\omega z/v}\left(\int_{-\infty}^{-z_0}dz'\,e^{i\omega z'/v}V_{r<a}^{\mathrm{out,ind}}(\mathbf{r},\mathbf{r}_0)+\int_{-z_0}^{z_0}dz'\,e^{i\omega z'/v}V_{r<a}^{\mathrm{in,ind}}(\mathbf{r},\mathbf{r}_0)\right.$$

$$+\int_{z_0}^{\infty}dz'\,e^{i\omega z'/v}V_{r<a}^{\mathrm{out,ind}}(\mathbf{r},\mathbf{r}_0)\Bigg)+\int_{z_0}^{\infty}dz\,e^{-i\omega z/v}\left(\int_{-\infty}^{-z_0}dz'\,e^{i\omega z'/v}V_{r>a}^{\mathrm{out,ind}}(\mathbf{r},\mathbf{r}_0)+\int_{-z_0}^{z_0}dz'\,e^{i\omega z'/v}V_{r>a}^{\mathrm{in,ind}}(\mathbf{r},\mathbf{r}_0)\right.$$

$$+\int_{z_0}^{\infty}dz'\,e^{i\omega z'/v}V_{r>a}^{\mathrm{out,ind}}(\mathbf{r},\mathbf{r}_0)\Bigg)\Bigg\}\Bigg|_{\mathbf{r}=(x_0,0,z')}\Bigg], \tag{33}$$

where the integration limit z_0 is given by $z_0=(a^2-x_0^2)^{1/2}$ if $x_0<a$ and $z_0=0$ if the electron is passing outside the sphere ($x_0>a$). After substitution of the expressions of the potential and some algebra, the excitation probability of the surface plasmon becomes

$$\frac{dP^{\mathrm{surf}}(\omega)}{d\omega}=-\frac{e^2}{4\pi^2\epsilon_0\hbar v^2 a}\sum_{l=0}^{\infty}\sum_{m=0}^{l}N_{l,m}(2-\delta_{0,m})$$

$$\times\mathrm{Im}[Q_{l,m}(\omega)]. \tag{34a}$$

For $l+m$ even, $Q_{l,m}(\omega)$ is given by

$$Q_{l,m}(\omega)=4\alpha_{l,m}(\omega)(\mathrm{Re}[F_{1,l}(\omega)])^2$$

$$+2\beta_{l,m}(\omega)\mathrm{Re}[F_{1,l}(\omega)]F_{2,l}(\omega)$$

$$+2\gamma_{l,m}(\omega)\mathrm{Re}[F_{1,l}(\omega)]F_{3,l}(\omega)+\sigma_{l,m}(\omega)$$

$$\times[F_{2,l}(\omega)]F_{3,l}(\omega), \tag{34b}$$

and for $l+m$ odd

$$Q_{l,m}(\omega)=4\alpha_{l,m}(\omega)(\mathrm{Im}[F_{1,l}(\omega)])^2$$

$$-2i\beta_{l,m}(\omega)\mathrm{Im}[F_{1,l}(\omega)]F_{2,l}(\omega)$$

$$+2i\gamma_{l,m}(\omega)\mathrm{Im}[F_{1,l}(\omega)]F_{3,l}(\omega)+\sigma_{l,m}(\omega)$$

$$\times[F_{2,l}(\omega)]F_{3,l}(\omega). \tag{34c}$$

The expression of the surface plasmon excitation probability [Eq. (34a)] incorporates the terms $\alpha_{l,m}(\omega)$, $\beta_{l,m}(\omega)$, $\gamma_{l,m}(\omega)$, and $\sigma_{l,m}(\omega)$ containing the different components of the dielectric tensor. They are defined as

$$\alpha_{l,m}(\omega) = \frac{l - \epsilon_\parallel(\omega) u_l^+(\omega)}{\epsilon_\parallel(\omega) u_l^+(\omega) + l + 1}, \quad (35a)$$

$$\beta_{l,m}(\omega) = \frac{2l+1}{\epsilon_\parallel(\omega) u_l^+(\omega) + l + 1}, \quad (35b)$$

$$\gamma_{l,m}(\omega) = \frac{(l+1)\epsilon_\perp(\omega) + \epsilon_\parallel(\omega) u_l^+(\omega)}{\epsilon_\perp(\omega)[\epsilon_\parallel(\omega) u_l^+(\omega) + l + 1]}, \quad (35c)$$

$$\sigma_{l,m}(\omega) = \frac{(l+1)(\epsilon_\perp(\omega) - 1)}{\epsilon_\perp(\omega)[\epsilon_\parallel(\omega) u_l^+(\omega) + l + 1]}. \quad (35d)$$

The different integrals appearing in Eq. (33) can be simplified so that only $F_{1,l}(\omega)$, $F_{2,l}(\omega)$, and $F_{3,l}(\omega)$ defined in Eqs. (36a)–(36c) remain:

$$F_{1,l}(\omega) = \int_{-\infty}^{-z_0} dz \left(\frac{a}{r}\right)^{l+1} P_{l,m}[\cos(\theta)] e^{-i\omega z/v}, \quad (36a)$$

$$F_{2,l}(\omega) = \int_{-z_0}^{z_0} dz \left(\frac{r}{a}\right)^{u_l^+(\omega)} P_{l,m}[\cos(\theta)] e^{-i\omega z/v}, \quad (36b)$$

$$F_{3,l}(\omega) = \int_{-z_0}^{z_0} dz \left(\frac{r}{a}\right)^l P_{l,m}[\cos(\theta)] e^{i\omega z/v}. \quad (36c)$$

It is worth noticing that when $\epsilon_\parallel(\omega) = \epsilon_\perp(\omega)$ (isotropic case) we find from Eqs. (34a)–(36c) the results of Bausell[39] (electron passing through an isotropic sphere) and Ferrell[38] or Echenique[37] (electron passing close to an isotropic sphere). Furthermore the polarizability of a nested concentric-shelled fullerene calculated by Lucas[20,21] is obtained from our results if one assumes that the electron passes outside the sphere.

C. Volume plasmon excitation

EELS measurements on uniaxial optical systems such as planar graphite have been carried out by Venghaus[52] and independently by Zeppenfeld.[53–55] The interpretation of the measurements, reviewed by Daniels *et al.*,[56] is based on the work of Hubbard,[57,58] Tosatti,[59] and Wessjohann.[49] For the determination of the volume plasmon excitation probability of an electron passing through an uniaxial crystal, the momentum transferred from a probe electron to the sample plays an important role. In typical TEM geometry, with an uniaxial crystal oriented in a way that its c axis is inclined by an angle α with respect to the optical axis of the microscope, the transferred momentum $\hbar \mathbf{q}$ can be expressed as a function of the scattering angle θ and the polar angle φ (see Fig. 3). The differential excitation probability as a function of the angles θ and φ can then be calculated. Since only electrons scattered within a angle smaller than the cutoff angle θ_c
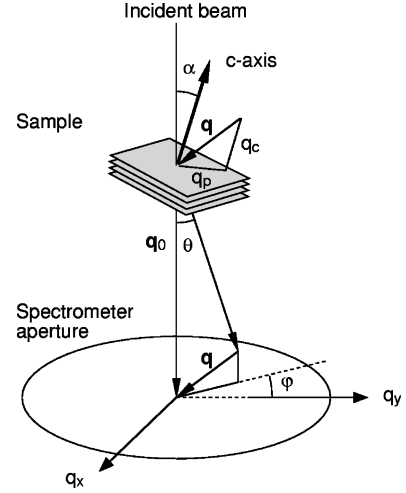

FIG. 3. Momentum transfer components for a TEM electron passing through a uniaxial crystal The c axis of the crystal is tilted by an angle α with respect to the incident electron beam. Before the scattering event, the electron has a momentum $\hbar \mathbf{q}_0$. During the scattering event, it transfers a momentum $\hbar \mathbf{q}$ to the crystal and is deviated by the scattering angle θ with respect to its incident direction and by the azimuthal angle φ.

(Ref. 60) contribute to the energy loss spectrum, the excitation probability per unit path length along the incident beam direction can be written as

$$\frac{d^2 P^{\text{volume}}(\omega)}{d\omega dz} = \frac{e^2}{4\pi^3 \epsilon_0 \hbar v^2} \int_0^{\theta_c} \theta d\theta \int_0^{2\pi} d\varphi$$

$$\times \text{Im}\left(\frac{-q_0^2}{q_p^2 \epsilon_\perp(\omega) + q_c^2 \epsilon_\parallel(\omega)}\right). \quad (37)$$

q_c and q_p are the projection of $\mathbf{q}$ onto the coordinate system in which the dielectric tensor is diagonal, i.e., on the unit vector parallel to the c axis of graphite and onto the plane perpendicular to the c axis, respectively (see Fig. 3). The two projections can be expressed in terms of the angles θ, φ, and α:

$$q_p^2 = q_0^2 \{[\theta_E \sin(\alpha) - \theta\cos(\varphi)\cos(\alpha)]^2 + [\theta\sin(\varphi)]^2\}, \quad (38a)$$

$$q_c^2 = q_0^2 \{[\theta_E \cos(\alpha) - \theta\cos(\varphi)\sin(\alpha)]^2\}. \quad (38b)$$

θ_E in Eqs. (39a) and (39b) is given by

$$\theta_E = \frac{\omega}{2\pi v q_0}. \quad (39)$$

Assuming local response, the energy loss of an electron penetrating through a graphitic carbon sphere can be calculated using Eq. (37). On each unit path length dz of the trajectory, the electron travels through a infinitely thin planar graphitic crystal with its c axis oriented radially at the position of the electron, as shown in Fig. 4.
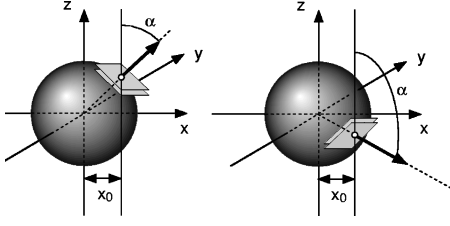
FIG. 4. Model for the determination of the volume plasmon excitation probability of an electron penetrating a multishell fullerene. On the infinitesimal path interval dz the electron travels through a uniaxial graphitic layer with its c axis oriented radially at the position of the electron. The orientation of the graphitic layers is shown for two different positions of the electron.

The angle α between the c axis of the oriented piece of graphite and the trajectory of the electron depends on the position of the electron. If the position is parametrized by z, then

$$\cos(\alpha) = \frac{z}{\sqrt{x_0^2 + z^2}}, \qquad (40a)$$

and

$$\sin(\alpha) = \frac{x_0}{\sqrt{x_0^2 + z^2}}. \qquad (40b)$$

The volume plasmon excitation probability of an electron penetrating a multishell fullerene can be obtained from Eq. (37) by numerical integration over the trajectory of the electron:

$$\frac{dP^{\text{volume}}(\omega)}{d\omega} = \int_{-z_0}^{z_0} dz \left(\frac{d^2 P^{\text{volume}}(\omega)}{d\omega dz} \right), \qquad (41)$$

where z_0 is given as before by $z_0 = (a^2 - x_0^2)^{1/2}$. With the explicit expression of the surface and volume plasmon excitation probabilities [Eqs. (34a)–(34c) and (41)] the total plasmon excitation probability is known:

$$\frac{dP^{\text{total}}(\omega)}{d\omega} = \frac{dP^{\text{volume}}(\omega)}{d\omega} + \frac{dP^{\text{surf}}(\omega)}{d\omega}. \qquad (42)$$

IV. RESULTS

A. General considerations

The expression of the plasmon excitation probability obtained in the previous paragraphs allows us to simulate two kinds of measurements that can be performed in an adequately equipped TEM. First, EEL spectra can be calculated for electrons passing at a given position when the impact parameter is kept fixed. Second, line scans across energy filtered images recorded at a given energy can be obtained when the energy loss probability is integrated over an energy window.

Excitation probabilities have been calculated using the MATHEMATICA software package of Wolfram Research Inc. We took into account neither the beam profile nor the energy spread of the probe electrons. Depending on the performance of the microscope, experimental spectra will therefore be
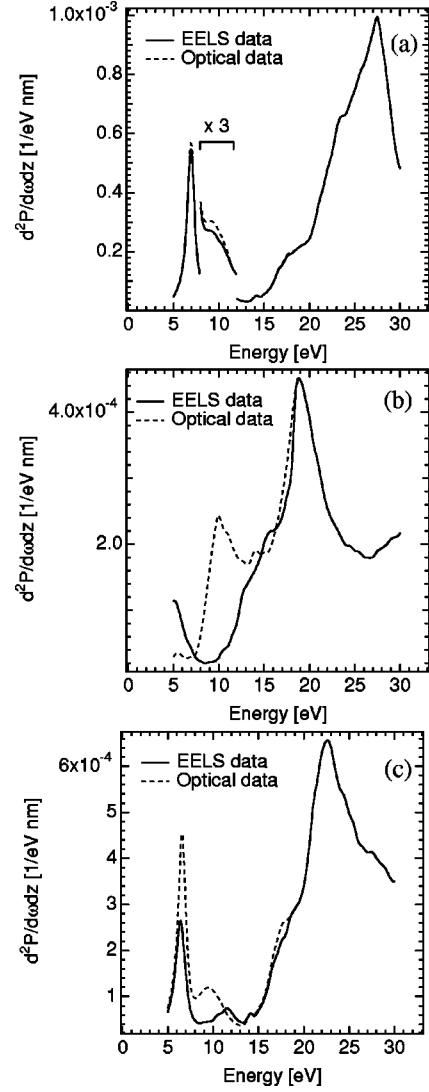

FIG. 5. Volume plasmon excitation probability per unit path length of planar graphite oriented with the c axis (a) parallel and (b) perpendicular to the optical axis of the microscope. The solid (dotted) curve is obtained from the dielectric tensor using EELS (optical) data. Graph (c) represents the volume plasmon excitation probability using an effective dielectric function as explained in the text.

broadened in comparison to our results. The simulations have been carried out for 100 keV beam electrons and for a cutoff angle θ_c of 50 mrad. The summation over the excitation modes has been carried out up to $l = 10$. Contributions of higher order modes turned out to be very small and did not significantly change position or intensity of the plasmon loss peaks.

The dielectric tensor of planar graphite needed for the description of the electronic properties of the multishell fullerene is taken from Ref. 61. There is, however, some discrepancy between the dielectric response of planar graphite for an electric field parallel to the c axis obtained from optical measurements[62,63] and from EELS measurements.[52,62] In Figs. 5(a) and 5(b) we compare EEL spectra of planar graphite for two orientations simulated using Eq. (37) and the different sets of data of the dielectric tensor. In Fig. 5(a) the graphite is oriented with its c axis parallel to the optical axis of the microscope ($\alpha = 0$). The dotted line is obtained

from optical data and the solid line from EELS data. The peaks at 7 and 27 eV are due to the collective excitation of the π electrons and the $\sigma + \pi$ electrons, respectively. It can be seen that for this orientation, the simulations with the two sets of data give almost identical results. In Fig. 5(b) the graphite is oriented with its c axis perpendicular to the electron beam ($\alpha = \pi/2$). Again, the dotted line is obtained from optical data and the solid one from EELS data. The absorption that can be observed between 15 and 20 eV is attributed to the excitation of interband transitions involving the three σ electrons per carbon atom.[64] For this orientation, there is a significant difference between the curves obtained from the different data. The peak at 11 eV that is present in the simulations with optical data is completely absent in the curve obtained from EELS data.

As a starting point for the discussion of our results we have simulated the excitation probability of an isotropic sphere assuming that the electronic properties of a multishell fullerene can be described by an effective dielectric function[65] $\epsilon_{\mathrm{eff}}(\omega) = (1/3)\epsilon_{\|}(\omega) + (2/3)\epsilon_{\perp}(\omega)$ (Sec. IV B 1). Figure 5(c) shows the volume plasmon excitation probability per unit path length obtained from Eq. (37) using $\epsilon_{\|}(\omega) = \epsilon_{\perp}(\omega) = \epsilon_{\mathrm{eff}}(\omega)$ with optical and with EELS data. In either case, three absorption peaks can be distinguished. Due to the mixing of the two components of the dielectric tensor of graphite, it is, however, not possible to associate them with any precise excitation mechanism. The main difference between the curves obtained from the two sets of data is that the absorption at 6.5 eV is less pronounced for EELS data as compared to optical data and that the small resonance at 11.5 eV in the case of EELS data is more intense and shifted to 10 eV in the case of optical data.

The simulated spectra presented in Secs. IV B 1 and IV B 2 have been calculated using optical data. However, since the disagreement over the dielectric tensor has not been settled up to now, we have also simulated spectra using EELS data (Sec. IV B 3).

B. Simulation of EEL spectra

1. Isotropic case (optical data)

Figure 6 shows the plasmon excitation probabilities obtained for electrons passing at different impact parameters through an isotropic sphere of 5 nm radius described by the effective dielectric function (optical data). In Fig. 6(a) the total excitation probability which can be compared to experimental data is displayed. In order to better understand the effect of the surface excitations, the surface plasmon excitation probability is shown separately in Fig. 6(b). It can be seen that the surface contribution is negative at certain energies. These negative contributions represent surface corrections to the bulk excitation probability[47,61] (Begrenzungseffect[66]). The negative terms naturally disappear when the electron passes outside the particle. Two distinct surface modes, one at 5.5 and the other at 17 eV, are excited [Fig. 6(b)]. When the electron passes through the center of the sphere, surface excitation induces two changes to the volume excitation [Fig. 5(c)]. The volume peak at 6.5 eV is broadened and a broad absorption feature at 17 eV appears. As the impact parameter is increased, the total excitation probability [Fig. 6(a)] changes due to the decrease of the volume contribution and to the increase of the surface contribution. The consequence is a further broadening of the 6.5 eV volume resonance peak and an increase of the intensity of the 17 eV surface peak. Finally, when the electron passes outside the sphere, only surface excitations remain.
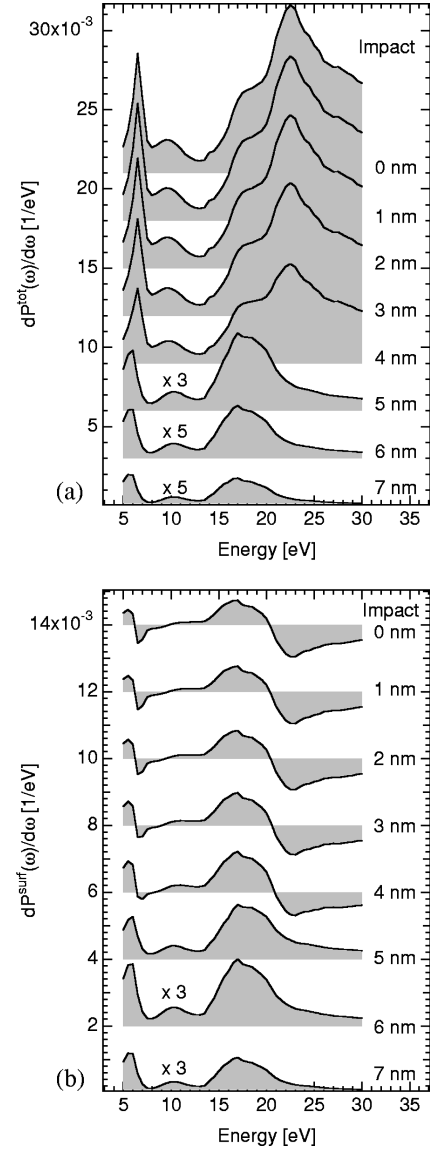

FIG. 6. (a) Total and (b) surface excitation probability for a sphere with a radius of 5 nm obtained with an effective dielectric function (optical data) for an isotropic sphere.

2. Anisotropic case (optical data)

Figure 7 shows the total (a) and surface (b) excitation probabilities for a sphere of 5 nm radius taking into account anisotropy (optical data). When the electron passes through the center of the sphere, it crosses graphitic layers oriented with the c axis parallel to the optical axis of the microscope and the total excitation probability [top curve of Fig. 7(a)] resembles the one of planar graphite oriented the same way [Fig. 5(a)]. The only noticeable difference is the broad feature at 17 eV which is due to surface excitations [compare to Fig. 7(b)]. When the impact parameter is increased, several important changes can be observed. The $\sigma + \pi$ electron vol-
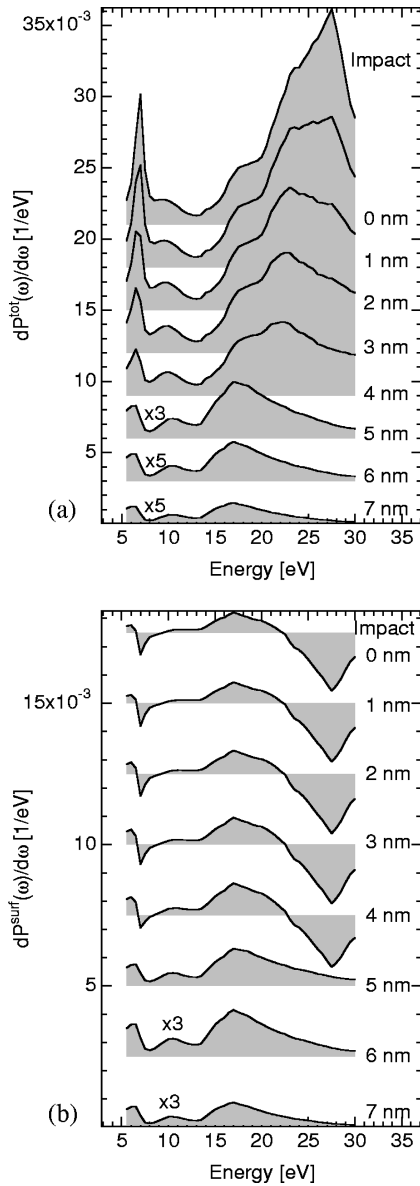
FIG. 7. (a) Total and (b) surface excitation probability for a sphere with a radius of 5 nm obtained with the dielectric tensor of graphite measured by an optical method.

ume plasmon resonance at 27 eV for an electron passing through the center appears to shift to 17 eV for an electron passing outside the particle. This shift can be explained by the combined action of several phenomena. First, there is a continuous change of the orientation of the graphitic layers towards the case where the electron only crosses graphitic layers oriented with the c axis perpendicular to the optical axis of the microscope (impact parameter approaching sphere radius). The excitation probability for an electron passing close to the interface through the particle resembles therefore the excitation probability shown in Fig. 5(b) with a resonance at 19 eV due to interband transitions of the σ electrons. Second, at the same time as the orientation changes, the path length inside the particle, and hence the intensity of the volume contribution, decreases and the surface contribution becomes more important [see Fig. 7(b)]. Overall, this leads to an apparent shift of the $\sigma + \pi$ electron

volume plasmon from 27 to 19 and finally to 17 eV when the electron passes outside the sphere.

The second feature that changes with the impact parameter is the π electron volume plasmon peak. It is shifted from 7 eV when the electron is passing at 0 nm impact parameter to 6 eV when the electron is passing close to the surface of the particle. At the same time the width of the loss peak is significantly broadened. The shifting and broadening of the π electron volume plasmon peak are due to the same phenomena described above, namely, the change in orientation of the graphitic layers, the shorter path inside the sphere, and the increase of the intensity of the surface excitations as the impact parameter is increased.

Compared to the simulations carried out within the isotropic restriction (Fig. 6), the simulations with the complete anisotropic formalism are different in two important aspects. First, in the isotropic case, the volume plasmon resonance peak at 23 eV remains at the same energy for any electron passing trough the sphere. In the anisotropic case, however, there is an apparent shift from 27 eV when the electron passes through the center of the sphere to 17 eV for an electron passing close to the surface. Second, in the anisotropic case, the π electron volume plasmon at 7 eV is broadened and shifted to 6 eV with increasing impact parameter. In the isotropic case the resonance at 6 eV is broadened, but not shifted.

In Fig. 8 the excitation probabilities for a sphere of 10 nm radius are shown. The difference between the simulations for the spheres of 5 nm and of 10 nm radii is the importance of the surface excitation probability as compared to the volume excitation probability. It turns out that the volume contribution of the sphere of 10 nm radius is twice the volume contribution of the sphere of 5 nm radius. At the same time the surface contribution is only increased by a factor of about 1.5 [Fig. 8(b)]. In Fig. 8(a) this is reflected in the fact that the surface resonance at 17 eV is weaker and that the broadening of the π plasmon resonance peak is less pronounced as in Fig. 7(a). Figure 8 gives therefore an impression of how the spectrum changes as a function of the impact parameter without hardly any surface effects.

3. Anisotropic case (EELS data)

If EELS data is used for the dielectric tensor, the simulations of the excitation probability for a sphere of 5 nm radius (Fig. 9) differ in one important aspect from the simulated spectra obtained from optical data (Fig. 7 and Fig. 8). The broad absorption figure at 11.5 eV that is visible for any impact parameter if optical data is used is much less pronounced. In the spectra resulting from simulations with EELS data the peak can only be seen if the electron passes close to the center of the sphere. When the electron passes close to the interface, the resonance is completely absent.

C. Simulations of energy filtered images

The second type of experiments that can be simulated with our model are energy filtered images. In such images the intensity recorded at a given position is the integral of the excitation probability over the experimental energy window at a given impact parameter. In Fig. 10 line scans simulated for an multishell fullerene of 5 nm radius are shown for an
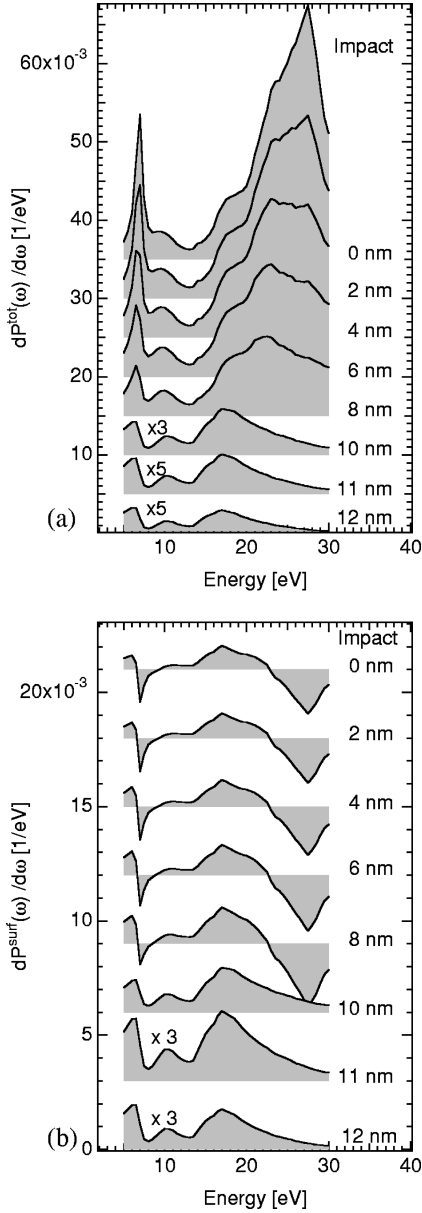
FIG. 8. (a) Total and (b) surface excitation probability for a sphere with a radius of 10 nm obtained with the dielectric tensor of graphite measured by an optical method.
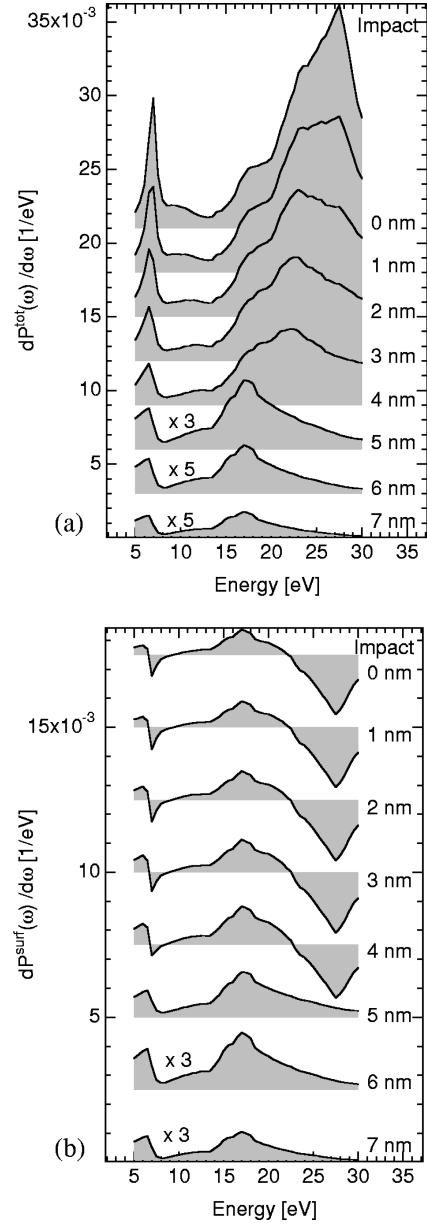

FIG. 9. (a) Total and (b) surface excitation probability for a sphere with a radius of 5 nm obtained with the dielectric tensor of graphite measured by EELS.

energy window of 3 eV centered at 7, 17, and 27 eV, respectively (optical data). The simulations show that the $\sigma + \pi$ electron volume plasmon at 27 eV is dominating in the center of the sphere (graphitic planes oriented with the c axis parallel to the incident electrons). The intensity at 27 eV decreases when the impact parameter is increased because of both the change in the orientation of the graphitic planes and the diminishing thickness as discussed in Sec. IV B 2. At 17 eV the intensity inside the particle remains almost constant. Again, this is due to the effect of a continuous change of orientation of the graphitic layers and the decrease in thickness as the sphere surface is approached. At this energy, however, the decrease in thickness is approximately compensated by the increasing intensity of surface excitations which explains the almost even intensity inside the sphere. Outside the particle the excitation probability at 17 eV drops less rapidly to zero than at 27 eV. This reveals the presence of

surface excitations, since only the surface resonance modes can be excited by electrons passing outside the particle. The line scan at 7 eV reflects the evolution of the π plasmon peak. The general tendency is similar to that of the line scan at 27 eV, although less pronounced. The evolution of this peak is mainly due to the change of orientation in the graphitic layers of the multishell fullerene. Eventhough surface effects are present in this energy range, the width of the energy window is too large to see them. The corrections to the volume peak due to surface excitation and the surface excitation itself are both in the energy window and compensate each other almost completely [see also Fig. 8(b)].

V. CONCLUSIONS

Local dielectric response theory, which has proven successful in explaining the plasmon losses of isotropic particles
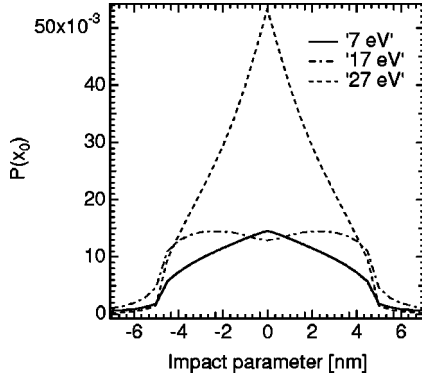
FIG. 10. Line scans across energy filtered images of a multishell fullerene of 5 nm radius simulated using the anisotropic model and optical data. The energy window was 3 eV wide and centered at 7, 17, and 27 eV.

of different geometry, has been adapted to take into account anisotropy as encountered in the case of nested concentric-shelled fullerenes. The calculations have been carried out for both penetrating and nonpenetrating electrons and allow the simulation of low loss EEL spectra and energy filtered images of this particular form of nanometer-size carbon particles. The simulations show that the inclusion of the anisotropy into the model is essential since important changes as compared to results of the isotropic model are observed.

In order to obtain a result suitable for numerical simulations we have made several assumptions in our approach. They can be classified into two categories. First, there are the approximations made in the frame of the local response theory, namely, the neglection of spatial dispersion and of relativistic effects such as retardation and Cerenkov radiation. More detailed calculations have shown that for spheres with radii between 2 and 20 nm the effects of retardation[67] and of spatial dispersion[68,69] can be neglected. Cerenkov radiation is negligible when $\epsilon(\omega)(v/c)^2 \gtrsim 1$, which is generally satisfied for metals (or semimetals) such as carbon. Local dielectric response is therefore adapted for multishell fullerenes with radii between 2 and 20 nm. The second category of assumptions arises from the description of the dielectric properties of multishell fullerenes based on the dielectric tensor of planar graphite. As a consequence, the effect of curvature on the local dielectric response is neglected and the possibility that the electronic properties of graphite could change if it is composed of very few layers is excluded.

The possibility to define a certain range of particle size in which local dielectric response theory has proven valid opens a way to experimentally investigate the influence of the second category of assumptions. This is highly interesting since they concern the intrinsic electronic properties of the multishell fullerenes. A detailed analysis of EEL data of multishell fullerenes of radii between 2 and 20 nm based on our simulations could therefore give important information on how the intrinsic electronic properties of this particular form of carbon differ from those of planar graphite.

ACKNOWLEDGMENTS

APPENDIX

The first of Maxwell's inhomogeneous equations relating the displacement vector to the charge density needs to be solved:

$$\nabla_{\mathbf{r}} \cdot \mathbf{D}(\mathbf{r},\mathbf{r}_0) = \rho(\mathbf{r},\mathbf{r}_0). \tag{A1}$$

Using the phenomenological relation between the displacement vector $\mathbf{D}(\mathbf{r},\mathbf{r}_0)$ and the electrical field $\mathbf{E}(\mathbf{r},\mathbf{r}_0)$, this relation becomes

$$\nabla_{\mathbf{r}} \cdot \epsilon_0 \widetilde{\epsilon}(\omega) \mathbf{E}(\mathbf{r},\mathbf{r}_0) = \rho(\mathbf{r},\mathbf{r}_0). \tag{A2}$$

The charge density due to the incident electron can be expressed via a Dirac function (point charge) $\rho(\mathbf{r},\mathbf{r}_0) = -e\,\delta(\mathbf{r}-\mathbf{r}_0)$. To solve this inhomogeneous differential equation we introduce the scalar function $\Phi(\mathbf{r},\mathbf{r}_0)$ defined by

$$\widetilde{\epsilon}(\omega) \mathbf{E}(\mathbf{r},\mathbf{r}_0) = -\nabla_{\mathbf{r}} \Phi(\mathbf{r},\mathbf{r}_0). \tag{A3}$$

Equation (A2) then becomes

$$\nabla_{\mathbf{r}}^2 \Phi(\mathbf{r},\mathbf{r}_0) = \frac{e}{\epsilon_0} \delta(\mathbf{r},\mathbf{r}_0). \tag{A4}$$

Formally this equation is identical to the Laplace equation. The function $\Phi(\mathbf{r},\mathbf{r}_0)$, however, is not the Coulomb potential, but only a mathematical construction introduced for convenience. From Eq. (A4) it is immediate that $\Phi(\mathbf{r},\mathbf{r}_0)$ is equal to

$$\begin{aligned}
\Phi(\mathbf{r},\mathbf{r}_0) &= -\frac{e}{4\pi\epsilon_0 |\mathbf{r}-\mathbf{r}_0|} \\
&= \frac{-e}{4\pi\epsilon_0} \sum_{l=0}^{\infty} \sum_{m=0}^{l} N_{l,m}(2-\delta_{0,m}) \\
&\quad \times P_{l,m}[\cos(\theta)] P_{l,m}[\cos(\theta_0)]\cos(m\varphi) \\
&\quad \times \begin{cases} \dfrac{1}{r_0}\left(\dfrac{r}{r_0}\right)^l & \text{for } r<r_0, \\[2ex] \dfrac{1}{r}\left(\dfrac{r_0}{r}\right)^l & \text{for } r>r_0, \end{cases}
\end{aligned} \tag{A5}$$

where $N_{l,m}=(l-m)!/(l+m)!$. With this expression for $\Phi(\mathbf{r},\mathbf{r}_0)$, the electric field $\mathbf{E}^{\text{in,p}}(\mathbf{r},\mathbf{r}_0)$ for a point charge in a infinitely large anisotropic medium can now be calculated using the gradient in spherical coordinates:

$$\begin{pmatrix} \epsilon_{\parallel}(\omega)E_r^{\text{in,p}} \\[1ex] \epsilon_{\perp}(\omega)E_\theta^{\text{in,p}} \\[1ex] \epsilon_{\perp}(\omega)E_\varphi^{\text{in,p}} \end{pmatrix} = \begin{pmatrix} \dfrac{\partial}{\partial r} \\[2ex] \dfrac{1}{r}\dfrac{\partial}{\partial\theta} \\[2ex] \dfrac{1}{r\sin(\theta)}\dfrac{\partial}{\partial\varphi} \end{pmatrix} \frac{e}{4\pi\epsilon_0|\mathbf{r}-\mathbf{r}_0|} \tag{A6}$$

and therefore

$$
\mathbf{E}_{r<a}^{\mathrm{in,p}}(\mathbf{r},\mathbf{r}_0)=\frac{e}{4\pi\epsilon_0}\sum_{l=0}^{\infty}\sum_{m=0}^{l}N_{l,m}(2-\delta_{0,m})P_{l,m}[\cos(\theta_0)]\left(\begin{array}{c}\dfrac{l}{\epsilon_\parallel(\omega)}\dfrac{r^{l-1}}{r_0^{l+1}}P_{l,m}[\cos(\theta)]\cos(m\varphi)\\[12pt]\dfrac{1}{\epsilon_\perp(\omega)}\dfrac{r^{l-1}}{r_0^{l+1}}\dfrac{\partial P_{l,m}[\cos(\theta)]}{\partial\theta}\cos(m\varphi)\\[12pt]-\dfrac{1}{\epsilon_\perp(\omega)}\dfrac{r^{l-1}}{r_0^{l+1}}\dfrac{1}{\sin(\theta)}P_{l,m}[\cos(\theta)]m\sin(m\varphi)\end{array}\right)\quad\text{(A7a)}
$$

for $r<r_0$ and

$$
\mathbf{E}_{r<a}^{\mathrm{in,p}}(\mathbf{r},\mathbf{r}_0)=\frac{e}{4\pi\epsilon_0}\sum_{l=0}^{\infty}\sum_{m=0}^{l}N_{l,m}(2-\delta_{0,m})P_{l,m}[\cos(\theta_0)]\left(\begin{array}{c}-\dfrac{l+1}{\epsilon_\parallel(\omega)}\dfrac{r_0^{l}}{r^{l+2}}P_{l,m}[\cos(\theta)]\cos(m\varphi)\\[12pt]\dfrac{1}{\epsilon_\perp(\omega)}\dfrac{r_0^{l}}{r^{l+2}}\dfrac{\partial P_{l,m}[\cos(\theta)]}{\partial\theta}\cos(m\varphi)\\[12pt]-\dfrac{1}{\epsilon_\perp(\omega)}\dfrac{r_0^{l}}{r^{l+2}}\dfrac{1}{\sin(\theta)}P_{l,m}(\cos(\theta))m\sin(m\varphi)\end{array}\right)\quad\text{(A7b)}
$$

for $r>r_0$.

*Electronic address: thomas.stoeckli@ipe.dp.epfl.ch

[1] H. W. Kroto, J. R. Health, S. C. O'Brian, R. F. Curl, and R. E. Smalley, Nature (London) **381**, 162 (1985).

[2] S. Iijima, Nature (London) **354**, 56 (1991).

[3] T. W. Ebbesen and P. M. Ajayan, Nature (London) **358**, 220 (1992).

[4] D. Ugarte, Nature (London) **359**, 707 (1992).

[5] S. Iijima and T. Ichihashi, Nature (London) **363**, 603 (1993).

[6] D. S. Bethune, C. H. Kiang, M. S. de Vries, G. Gorman, R. Savoy, J. Vazquez, and R. Beyers, Nature (London) **363**, 605 (1993).

[7] W. Krätschmer, L. D. Lamb, K. Fostiropoulos, and D. R. Huffman, Nature (London) **347**, 354 (1990).

[8] J.-M. Bonard, T. Stora, J.-P. Salvetat, F. Maier, T. Stöckli, C. Duschl, L. Forró, W. de Heer, and A. Châtelain, Adv. Mater. **9**, 827 (1997).

[9] A. Thess, R. Lee, P. Nikolaev, H. Dai, P. Petit, J. Robert, Ch. Xu, Y. H. Lee, S. G. Kim, D. T. Colbert, G. Scuseria, D. Tomanek, J. E. Fischer, and R. E. Smalley, Science **273**, 483 (1996).

[10] C. Journet, W. K. Maser, P. Bernier, A. Loiseau, M. Lamy de la Chapelle, S. Lefrant, P. Deniard, R. Lee, and j. E. Fischer, Nature (London) **388**, 756 (1997).

[11] J. P. Lu, Phys. Rev. Lett. **74**, 1123 (1995).

[12] P. J. Lin-Chung and A. K. Rajagopal, Phys. Rev. B **49**, 8454 (1994).

[13] N. Hamada, S. Sawada, and A. Oshiyama, Phys. Rev. Lett. **68**, 1579 (1992).

[14] J. W. Mintmire, B. I. Dunlap, and C. T. White, Phys. Rev. Lett. **68**, 631 (1992).

[15] R. Saito, G. Fujita, G. Dresselhaus, and M. S. Dresselhaus, Appl. Phys. Lett. **60**, 2204 (1992).

[16] M. F. Lin and K. W.-K. Shung, Phys. Rev. B **50**, 17 744 (1994).

[17] C. Yannouleas, E. N. Bogachek, and U. Landman, Phys. Rev. B **50**, 7977 (1994).

[18] C. Yannouleas, E. N. Bogachek, and U. Landman, Phys. Rev. B **53**, 10 225 (1996).

[19] L. Henrard and P. Lambin, J. Phys. B **29**, 5129 (1996).

[20] A. A. Lucas, L. Henrard, and P. Lambin, Phys. Rev. B **49**, 2888 (1994).

[21] A. A. Lucas, L. Henrard, and P. Lambin, Nucl. Instrum. Methods Phys. Res. B **96**, 465 (1995).

[22] R. P. Diez, M. P. Iniguez, M. J. Scott, and J. A. Alonso, Phys. Rev. B **52**, 8446 (1995).

[23] X. Blase, L. X. Benedict, E. L. Shirley, and S. G. Louie, Phys. Rev. Lett. **72**, 1878 (1994).

[24] J.-M. Bonard, T. Stöckli, W. A. de Heer, A. Châtelain, J.-C. Charlier, X. Blase, A. De Vita, R. Car, J.-P. Salvetat, and L. Forró, Phys. Rev. Lett. (to be published).

[25] S. J. Tans, M. H. Devoret, H. Dai, A. Thess, R. E. Smalley, L. J. Geerligs, and C. Dekker, Nature (London) **386**, 474 (1997).

[26] D. L. Carroll, P. Redlich, P. M. Ajayan, J. C. Charlier, X. Blase, A. De Vita, and R. Car, Phys. Rev. Lett. **78**, 2811 (1997).

[27] P. M. Ajayan, S. Iijima, and T. Ichihashi, Phys. Rev. B **47**, 6859 (1992).

[28] L. A. Bursill, P. A. Stadelmann, J. L. Peng, and S. Prawer, Phys. Rev. B **49**, 2882 (1992).

[29] R. Kuzuo, M. Terauchi, and M. Tanaka, Jpn. J. Appl. Phys., Part 2 **31**, L1484 (1992).

[30] K. Yase, S. Horiuchi, M. Kyotani, M. Yumura, K. Uchida, S. Ohshima, Y. Kuriki, F. Ikazaki, and N. Yamahira, Thin Solid Films **273**, 222 (1996).

[31] T. Stöckli, J.-M. Bonard, P. A. Stadelmann, and A. Châtelain, Z. Phys. D **40**, 425 (1997).

[32] O. Stéphan, P. M. Ajayan, C. Colliex, F. Cyrot-Lackmann, and E. Sandré, Phys. Rev. B **53**, 13 824 (1996).

[33] P. Apell and D. Östling, Solid State Commun. **87**, 219 (1993).

[34] Z. L. Wang, Micron **27**, 265 (1996).

[35] R. H. Ritchie, Phys. Rev. **106**, 874 (1957).

[36] T. L. Ferrell and P. M. Echenique, Phys. Rev. Lett. **55**, 1526 (1985).

[37] M. Echenique, A. Howie, and D. J. Wheatley, Philos. Mag. B **56**, 335 (1987).

[38] T. L. Ferrell, R. J. Warmack, V. E. Anderson, and P. M. Echenique, Phys. Rev. B **35**, 7365 (1987).

[39] J. Bausells, A. Rivacoba, and P. M. Echenique, Surf. Sci. **190**, 1015 (1987).

[40] D. Ugarte, C. Colliex, and P. Trebbia, Phys. Rev. B **45**, 4332 (1992).

[41] T. Stöckli, P. Stadelmann, and A. Châtelain, Microsc. Microanal. Microstruct. **8**, 145 (1997).

[42] Z. L. Wang and J. M. Cowley, Ultramicroscopy **21**, 347 (1987).

[43] N. Zabala and A. Rivacoba, Ultramicroscopy **35**, 145 (1991).

[44] C. A. Walsh, Philos. Mag. B **63**, 1063 (1991).

[45] N. Zabala, A. Rivacoba, and P. M. Echenique, Surf. Sci. **209**, 465 (1989).

[46] Y. T. Chu, R. J. Warmack, R. H. Ritchie, J. W. Little, R. S. Becker, and T. L. Ferrell, Part. Accel. **16**, 13 (1984).

[47] A. Rivacoba, P. Apell, and N. Zabala, Nucl. Instrum. Methods Phys. Res. B **96**, 470 (1995).

[48] Z. L. Wang, *Elastic and Inelastic Scattering in Electron Diffraction and Imaging* (Plenum, New York, 1995).

[49] H. G. Wessjohann, Z. Phys. **26**, 269 (1974).

[50] W. R. Smythe, *Static and Dynamic Electricity* (McGraw-Hill, New York, 1939).

[51] J. D. Jackson, *Classical Electrodynamics* (Wiley, New York, 1975).

[52] H. Venghaus, Phys. Status Solidi B **71**, 609 (1975).

[53] K. Zeppenfeld, Phys. Lett. **25A**, 335 (1967).

[54] K. Zeppenfeld, Opt. Commun. **1**, 119 (1969).

[55] K. Zeppenfeld, Z. Phys. **211**, 391 (1968).

[56] J. Daniels, C. Festenberg, H. Raether, and K. Zeppenfeld, in *Optical Constants of Solids by Electron Spectroscopy*, edited by G. Höhler (Springer, Berlin, 1979).

[57] J. Hubbard, Proc. Phys. Soc. London, Sect. A **68**, 976 (1955).

[58] J. Hubbard, Proc. Phys. Soc. London, Sect. A **68**, 441 (1955).

[59] E. Tosatti and F. Bassani, Nuovo Cimento B **65**, 161 (1970).

[60] R. F. Egerton, *Electron Energy Loss Spectroscopy in the Electron Microscope* (Plenum, New York, 1989).

[61] A. Rivacoba, J. Aizpurua, and N. Zabala, Scanning Microsc. **9**, 927 (1995).

[62] *Handbook of Optical Constants of Solids*, edited by E. D. Palik (Academic, New York, 1985).

[63] R. Klucker (unpublished).

[64] E. A. Taft and H. R. Philipp, Phys. Rev. **138**, A197 (1965).

[65] B. T. Draine and H. M. Lee, Astrophys. J. **285**, 89 (1984).

[66] H. Boersch, J. Geiger, and W. Stickel, Z. Phys. **212**, 130 (1968).

[67] A. D. Boardman and B. D. Paranjape, J. Phys. F **7**, 1935 (1977).

[68] Z. L. Wang and J. M. Cowley, Ultramicroscopy **23**, 97 (1987).

[69] R. Ruppin, J. Phys. Chem. Solids **39**, 233 (1978).